



Cite this: *Phys. Chem. Chem. Phys.*,  
2021, 23, 7418

## Band alignment of monolayer $\text{CaP}_3$ , $\text{CaAs}_3$ , $\text{BaAs}_3$ and the role of p–d orbital interactions in the formation of conduction band minima<sup>†</sup>

Magdalena Laurien,<sup>ID\*</sup> Himanshu Saini<sup>ID</sup> and Oleg Rubel<sup>ID\*</sup>

Recently, a number of new two-dimensional (2D) materials based on puckered phosphorene and arsenene have been predicted with moderate band gaps, good absorption properties and carrier mobilities superior to those of transition metal dichalcogenides. For heterojunction applications, it is important to know the relative band alignment of these new 2D materials. We report the band alignment of puckered  $\text{CaP}_3$ ,  $\text{CaAs}_3$  and  $\text{BaAs}_3$  monolayers at the quasiparticle level of theory ( $G_0W_0$ ), calculating band offsets for isolated monolayers according to the electron affinity rule. Our calculations suggest that monolayer  $\text{CaP}_3$ ,  $\text{CaAs}_3$  and  $\text{BaAs}_3$  all form type-II (staggered) heterojunctions which makes them suitable for solar-energy conversion applications. Their quasiparticle gaps are 2.1 (direct), 1.8 (direct) and 1.5 eV (indirect), respectively. We also examine trends in the electronic structure in the light of chemical bonding analysis. We show that the indirect band gap in monolayer  $\text{BaAs}_3$  is caused by relatively strong As 3p–Ba 5d bonding interactions. Our results provide guidance for the design of phosphorene-like materials and their heterojunction applications.

Received 8th January 2021,  
Accepted 8th March 2021

DOI: 10.1039/d1cp00099c

rsc.li/pccp

### 1 Introduction

The optical and electronic properties of black phosphorus (bP), such as its high carrier mobility<sup>1</sup> and tunable band gap,<sup>2</sup> have sparked interest in the broader family of phosphorene related 2D material structures. Recently, several new 2D materials related to phosphorene and arsenene – for which a part of the As or P atoms is replaced by group II elements<sup>3–5</sup> or elements of other groups (III, IV, or V)<sup>6–9</sup> – have been predicted. These layered materials show a combination of high carrier mobilities, moderate band gaps and good light absorption properties promising for next-generation electronic heterojunction devices like solar cells and transistors.

For example, monolayer (1L)  $\text{CaP}_3$  is predicted to have a band gap of 1.15 eV<sup>5</sup> (using a hybrid functional, HSE06) and a high electron mobility of up to *ca.* 20 000 cm<sup>2</sup> V<sup>-1</sup> s<sup>-1</sup> (using deformation potential theory, values need to be taken with caution as

deformation potential theory usually overestimates mobility values<sup>10,11</sup>).

For materials selection in heterojunction design, it is necessary to know the band alignments of the layered structures. However, band alignments for novel 2D materials of the phosphorene family have not yet been reported and the majority of the band gaps of these 2D structures have been calculated using hybrid functionals at the density functional level of theory (DFT). Although hybrid functionals alleviate the band gap problem of DFT, it is generally accepted that GW quasiparticle calculations provide the most reliable and accurate level of theory for band structure and band alignment calculations.<sup>12–15</sup>

Here, we calculate the band gaps of the recently predicted<sup>3–5</sup>  $\text{CaP}_3$ ,  $\text{CaAs}_3$  and  $\text{BaAs}_3$  monolayers at the  $G_0W_0$  level of theory. We estimate their band alignments according to the electron affinity rule which states that the conduction band offset of a heterojunction can be obtained from the electron affinities of the individual materials. Analyzing the electron affinity of the isolated monolayers is a valid first step in materials selection process for possible 2D heterostructures.<sup>16,17</sup> Furthermore, we explain the differences in band alignment based on structure analysis and show that the indirect nature of the band gap in 1L  $\text{BaAs}_3$  is caused by increasing p–d orbital interactions. Our analysis sheds light on the influence of structure and orbital interactions on the theoretical band offsets in phosphorene-like materials. These insights may be helpful for the design of phosphorene-like materials and their heterojunctions.

Department of Materials Science and Engineering, McMaster University,  
1280 Main Street West, Hamilton, Ontario L8S 4L7, Canada.

E-mail: laurienm@mcmaster.ca, rubelo@mcmaster.ca

<sup>†</sup> Electronic supplementary information (ESI) available: VASP structure files (POSCAR). Band structures plotted from Wannier functions *versus* band structures along a *k*-path from DFT (Fig. S1–S3). Band alignment of a  $\text{CaAs}_3/\text{CaP}_3$  heterostructure (Fig. S4 and S5). Projected charge density of monolayer  $\text{CaAs}_3$ , monolayer  $\text{BaAs}_3$  and monolayer  $\text{CaP}_3$  (Fig. S6–S9). COHP analysis for puckered arsenene and phosphorene (Fig. S10 and S11). See DOI: 10.1039/d1cp00099c

## 2 Methods

### 2.1 Structural relaxation (DFT)

First, we relaxed the experimental bulk structures of  $\text{CaAs}_3$ ,<sup>18</sup>  $\text{CaP}_3$ ,<sup>19</sup> and  $\text{BaAs}_3$ .<sup>18</sup> The structures were relaxed on the DFT level using the Vienna *ab initio* package (VASP)<sup>20,21</sup> with projector-augmented potentials<sup>22</sup> as implemented by Kresse and Joubert.<sup>23</sup> We explicitly included eight valence and core electrons for Ca, ten electrons for Ba, 15 electrons for As and five valence electrons for P. The Perdew–Burke–Ernzerhof (PBE)<sup>24</sup> exchange–correlation functional with D3 van der Waals corrections<sup>25</sup> was used to obtain the electronic ground state. We used a  $k$  grid sampling of  $6 \times 6 \times 6$  and a plane-wave-expansion cutoff of 550 eV. The structures were fully relaxed until the residual atomic forces were less than 0.001 eV Å<sup>-1</sup>. From these, monolayer structures were obtained and subsequently relaxed using VASP. We used a  $6 \times 6 \times 1$   $k$  grid and fixed the out-of-plane lattice parameter  $c$  during the relaxation procedure. To avoid interactions between periodic images, we included a vacuum of at least 22.5 Å in the out-of-plane direction. The POSCAR structure files of the relaxed monolayers are included in the ESI.†

The rationale for our choice of the functional and van der Waals correction was to get a relaxed bulk structure that is as close as possible to that obtained in experiment. Relaxation with PBE-D3 resulted in a bulk structure closest to experiment while PBE-VV10 with non-local van der Waals corrections<sup>26</sup> gave a structure farthest from experiment among the functionals tested. 1L  $\text{CaAs}_3$  obtained from the PBE-VV10 relaxed bulk structure and relaxed with PBE-VV10 had a PBE band gap that was 25% smaller than that of the PBE-D3 structure.

### 2.2 $G_0W_0$ calculations

As input for the GW calculations, we computed DFT wavefunctions and eigenvalues using the Quantum Espresso (QE) code.<sup>27</sup> QE band structure calculations were performed for the relaxed monolayer structures with PBE and norm-conserving pseudopotentials,<sup>28</sup> using a plane-wave energy cutoff of 116 Ry and  $k$  grid of  $12 \times 12 \times 1$ . We included ten valence and semicore states for Ca and Ba, 15 states for As and five valence states for P. The vacuum included for the QE and subsequent calculations was smaller than that during the structural relaxation and was sufficient to contain at least 99% of the charge density in half the unit cell. We neglected spin orbit coupling in our calculations as it was shown by Tang *et al.*<sup>3</sup> that including relativistic effects changes the band gap by less than 0.01 eV in monolayer  $\text{BaAs}_3$ .

Subsequently, we performed “single-shot”  $G_0W_0$  calculations using the BerkeleyGW software.<sup>29–31</sup> We employed the generalized plasmon-pole model,<sup>29</sup> the static-remainder technique,<sup>32</sup> and truncation of the long-range Coulomb interaction.<sup>33</sup> We used a  $k$  point sampling of  $6 \times 6 \times 1$  and a kinetic energy cutoff of 20 Ry. About 1000 bands were included for the calculation of the dielectric function as well as for the calculation of the self-energy. To speed up the convergence of the quasiparticle band gap with respect to  $k$  grid sampling, we employed nonuniform-neck subsampling<sup>34</sup> with 10 radial subpoints. The convergence was

tested for the  $\text{CaAs}_3$  monolayer as a representative material. The quasiparticle band gap at  $\Gamma$  was converged within 0.05 eV with respect to calculations with a kinetic cutoff of 40 Ry and 3000 bands in the summations, and a calculation with a  $12 \times 12 \times 1$   $k$  point grid plus 10 subpoints.

To verify our approach, we also calculated the quasiparticle band gaps (not to be confused with the optical band gap where excitonic effects contribute a significant correction) of the parent structures, puckered phosphorene and arsenene, using the same parameters. We obtained a band gap of 2.02 eV for phosphorene and 1.84 eV for arsenene. The value of phosphorene is in excellent agreement with other theoretical (Qiu *et al.*:<sup>35</sup> 2.08 eV, da jornada *et al.*:<sup>34</sup> 2.05 eV, Lu *et al.*:<sup>36</sup> 2.0 eV), and experimental studies (Liang *et al.*:<sup>37</sup> using scanning tunneling spectroscopy: 2.05 eV). For puckered arsenene, experimental quasiparticle gaps are not available and theoretical band gaps vary between 1.54 eV,<sup>38</sup> 1.58 eV<sup>39</sup> and 2.16 eV.<sup>40</sup> The discrepancies may, among other factors, be attributed to structural differences, as the experimental structures of both 1L and bulk puckered arsenene, which would serve as the starting point for DFT calculations, are still lacking.

The  $G_0W_0$  band structure was obtained from Wannier interpolation using the wannier90 package.<sup>41</sup> A comparison of the directly calculated and interpolated PBE band structure is shown in the ESI,† Fig. S1–S3, to illustrate the accuracy of the interpolation. The wannierization was performed for 100 iterations using random projections with 40 bands (20 valence and 20 conduction bands, each) as input to obtain 40 Wannier functions.

### 2.3 Data analysis

Crystal structures were visualized using VESTA.<sup>42</sup> The Brillouin zone was visualized using XCrySDen.<sup>43</sup> The partial density of states (pDOS) and the projected charge density were obtained using VASP with the PBE exchange–correlation functional. The potential in a vacuum was calculated at the DFT-PBE-D3 level using the vasplkit tool.<sup>44</sup> We note that the vacuum level offset varies depending on the functionals used for structural relaxation. Using the PBE-VV10 functional (see above) we obtained absolute midgap levels for 1L  $\text{CaAs}_3$  which were about 0.6 eV lower than those using the PBE-D3 functional, which is a difference of 25%.

We estimated the  $G_0W_0$  band alignment (electron affinity) with respect to the vacuum of each monolayer using the band-gap-center approximation:<sup>45</sup>

$$E_{\text{EA}} \approx \frac{1}{2}(E_{\text{c}}^{\text{DFT-PBE}} + E_{\text{v}}^{\text{DFT-PBE}}) + \frac{1}{2}E_{\text{g}}^{G_0W_0}, \quad (1)$$

which is equivalent to shifting the band edges of the PBE bands by  $\pm(E_{\text{g}}^{G_0W_0} - E_{\text{g}}^{\text{DFT-PBE}})/2$ . We note that the band-gap-center approximation works well for PBE centers and  $G_0W_0$  gaps; however, it does not hold for results obtained with hybrid functionals.<sup>46,47</sup>

To estimate the heterojunction type (*e.g.* straddled or staggered gap) between the isolated monolayers, we applied Anderson’s electron affinity rule.<sup>48</sup> The electron affinity rule implies that the conduction band offset of a heterojunction can be obtained by

16 and experimentally<sup>17</sup> that the band alignment follows the electron affinity rule for vertically stacked heterostructures of transition metal dichalcogenides. This behaviour is attributed to the weak van der Waals bonding across the interface and the absence of dangling bonds in 2D materials.<sup>16,17</sup> Now, phosphorene and arsenene related materials are expected to have stronger interlayer interactions than transition metal dichalcogenides, which is indicated by the rapid decrease of the band gap with the number of layers. Therefore, the heterojunction predictions from the electron affinity rule need to be taken with caution. With interlayer interactions turned on, the band offsets can change due to charge transfer across the layer and band mixing may occur.<sup>15,49</sup>

To estimate the effect of charge transfer and band shifts in a heterojunction, we calculated the band alignment of a basic  $\text{CaAs}_3/\text{CaP}_3$  heterostructure at the PBE level using VASP and pyprocar<sup>50</sup> (see ESI,† Fig. S4 and S5). Our results predict that the band gaps and relative band alignments of the monolayers are only slightly affected by creating a heterostructure. Despite charge transfer and weak to moderate hybridization of the conduction bands, the electron affinity rule gives a good estimate of the band alignment of the heterostructure.

## 3 Results and discussion

### 3.1 Structure and bonding

Fig. 1(a–c) shows the atomic structure and Brillouin zone of 1L  $\text{CaAs}_3$  as an example structure of the  $\text{CaP}_3$  family. The Ca atom replaces one quarter of the As atoms in the puckered structure of puckered arsenene. 1L  $\text{CaP}_3$  and 1L  $\text{BaAs}_3$  are also shown in Fig. 1(d) and (e). 1L  $\text{CaP}_3$  and 1L  $\text{CaAs}_3$  inherit the  $\bar{P}1$  space

group from the corresponding bulk structures. 1L  $\text{BaAs}_3$  possesses higher symmetry and belongs to the  $C2/m$  space group same as its bulk structure.

In pristine arsenene, the As atoms form covalent bonds. For 1L  $\text{CaAs}_3$ , the Ca atom is stabilized by ionic interactions between the Ca cation and the anionic As mesh.<sup>4</sup> We note that one can distinguish between two types of As atoms (see Fig. 1(b)): As1 which is further away from the Ca atoms, and As2 which is closer to the Ca atoms with As2 having a more negative partial charge than As1.<sup>4</sup> (We note here that atoms belonging to each type are not necessarily symmetrically identical; they are only equivalent for  $\text{BaAs}_3$ .) These considerations hold true in analogy for  $\text{BaAs}_3$  and  $\text{CaP}_3$ .

### 3.2 Band alignment

The band alignments of monolayer  $\text{CaP}_3$ ,  $\text{CaAs}_3$  and  $\text{BaAs}_3$  obtained from  $G_0W_0$  calculations with the band-gap center approximation are shown in Fig. 2. The  $G_0W_0$  gaps of 1L  $\text{CaP}_3$ ,  $\text{CaAs}_3$  and  $\text{BaAs}_3$  are 2.11 eV, 1.79 eV and 1.50 eV, respectively. Phosphorene ("P<sub>4</sub>") and arsenene ("As<sub>4</sub>") have been added for comparison. Direct and indirect band gaps are signified by dark and light blue colors, respectively. The band alignment diagram shows that, according to the electron affinity rule, 1L  $\text{CaP}_3$ ,  $\text{CaAs}_3$  and  $\text{BaAs}_3$  form type-II (staggered) heterojunctions. Between the pristine monolayers and the compound monolayers, the 1L-bP/1L-CaP<sub>3</sub> and 1L-bP/1L-BaAs<sub>3</sub> combinations are predicted to have broken-gap band alignment (type III) whereas the other combinations show type-II alignments. Type-II heterojunctions are of interest for solar cell applications because they enable charge separation of photoinduced electrons and holes across the junction.<sup>51</sup> The narrow type-II and type-III alignments of the potential 1L-bP/1L-CaX<sub>3</sub> and 1L-arsenene/1L-CaX<sub>3</sub> (X = As, P) heterojunctions suggest promising material combinations for tunneling field effect transistor applications.<sup>52</sup> Such devices

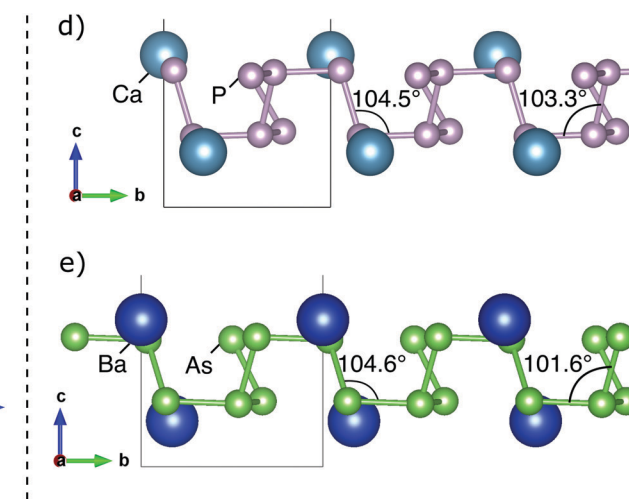
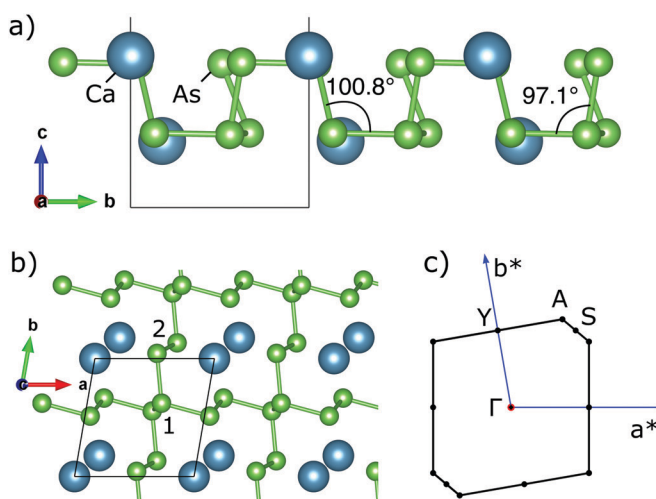


**Fig. 1** Structure of the  $\text{CaAs}_3$ ,  $\text{CaP}_3$  and  $\text{BaAs}_3$  monolayer. (a) 1L  $\text{CaAs}_3$  as a representative compound shows a puckered configuration similar to arsenene where one quarter of As atoms is replaced with Ca, the other As atoms forming a polyanionic network. (b) Top view of the  $\text{CaAs}_3$  monolayer. The numbers 1 and 2 refer to two structural types of As atoms (see the main text for details) (c) Brillouin zone of the  $\text{CaAs}_3$  monolayer. The structures of monolayer  $\text{CaP}_3$  (d) and  $\text{BaAs}_3$  (e) are added to show the distinct structural distortion of each material.

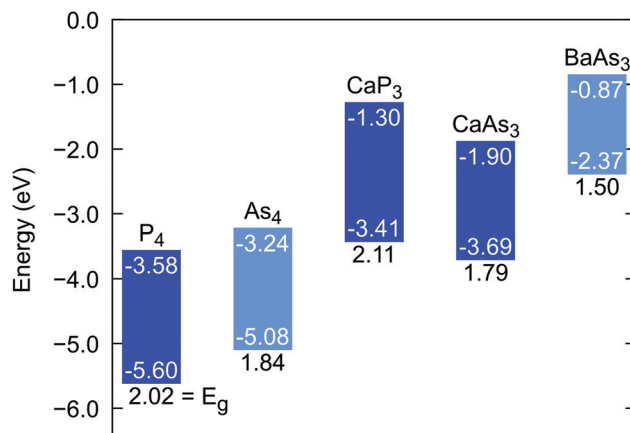


**Fig. 2** Band alignment of isolated monolayer  $\text{CaP}_3$ ,  $\text{CaAs}_3$  and  $\text{BaAs}_3$  with respect to the vacuum level (0 eV). Band energies and offsets are obtained from  $G_0W_0$  calculations with the band-gap center approximation (eqn (1)). Band gaps and alignment of black phosphorene ( $\text{P}_4$ ) and arsenene ( $\text{As}_4$ ) have been added for reference. Indirect band gaps are indicated by light blue color, direct band gaps correspond to dark blue.

would benefit from the high carrier mobilities predicted for the monolayers of the  $\text{CaP}_3$  family as well as from the very easily tunable band gap. We note that for real heterojunctions with enabled interlayer interactions, the band offsets may change due to the following effects: charge transfer across the interface, band mixing, and changes in the band gap.<sup>15,49</sup>

We will now analyze the calculated band alignments in further detail. Looking at the band alignment (Fig. 2), it becomes apparent that monolayer  $\text{CaP}_3$ ,  $\text{CaAs}_3$  and  $\text{BaAs}_3$  have considerably smaller conduction band offsets with respect to the vacuum level than pure arsenene and phosphorene. Ca and Ba as group-II elements have much lower electron affinities than the group-V elements (As and P) thus leading to a higher energy of the conduction band edge in these compounds. Between monolayer  $\text{CaAs}_3$  and  $\text{BaAs}_3$ , the midgap of  $\text{CaAs}_3$  is lower in energy than for  $\text{BaAs}_3$  (Fig. 2). The reason for this energy difference is not apparent at first sight. Therefore, we included a hypothetical  $\text{SrAs}_3$  monolayer to analyze

the trend. As the alkaline metal atom becomes heavier, the conduction band minimum (CBM) shifts more toward the vacuum level.

To differentiate between effects of the chemical composition and structural effects, we swapped the Ca atoms of the 1L  $\text{CaAs}_3$  structure with Ba atoms and *vice versa* without a subsequent relaxation of atomic positions or lattice parameters. We found that inserting Ca into the  $\text{BaAs}_3$  structure shifted the CBM away from the vacuum level. Inserting Ba into the  $\text{CaAs}_3$  structure shifted the CBM towards the vacuum level. From our data (not shown), we concluded that the band alignment offset between 1L  $\text{CaAs}_3$  and 1L  $\text{BaAs}_3$  is half due to structural effects and half due to the effects of the chemical composition. Structural differences include a stretching of the puckered structure of 1L  $\text{BaAs}_3$  within the plane in comparison to 1L  $\text{CaAs}_3$  as the angles between the As atoms in the puckered mesh are greater for 1L  $\text{BaAs}_3$ . Also, the Ba atoms stick out of the monolayer plane more than the Ca atoms because of their larger atomic radius (compare Fig. 1a and e).

Interestingly, the band edges of 1L  $\text{CaP}_3$  are higher in energy than the ones of 1L  $\text{CaAs}_3$  although the midgap energy of phosphorene is lower than that of arsenene (see Fig. 2). Swapping P for As in 1L  $\text{CaAs}_3$  and As for P in 1L  $\text{CaP}_3$  did not affect the band offset with respect to the vacuum level much. Thus, we can conclude that the offset of the band edges is less influenced by the pnictogen and is likely caused by structural distortions. For example, the P-P bond length of 2.22 Å on average in 1L  $\text{CaP}_3$  is much shorter than the As-As bond in 1L  $\text{CaAs}_3$  with 2.50 Å and, as a result, the Ca atoms “stick out” of the monolayer much more than in 1L  $\text{CaAs}_3$  (see Fig. 1d). The puckered mesh also shows larger angles than in 1L  $\text{CaAs}_3$ .

### 3.3 Electronic structure, the effect of p-d interactions

We further explore and analyze the band structure and projected density of states (pDOS), pointing to trends from chemical bonding analysis. The PBE and  $G_0W_0$  band structures of 1L  $\text{CaP}_3$ , 1L  $\text{CaAs}_3$  and 1L  $\text{BaAs}_3$  obtained by Wannier interpolation are shown in Fig. 3. 1L  $\text{CaP}_3$  and 1L  $\text{CaAs}_3$  have a direct band gap

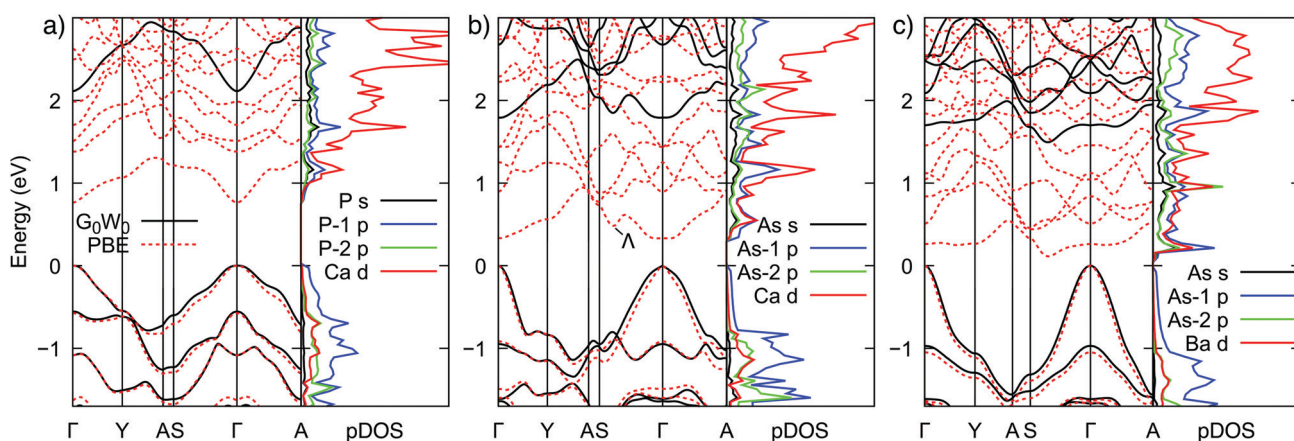


**Fig. 3** GW and PBE band structures from Wannier interpolation and projected density of states (pDOS) of (a) monolayer  $\text{CaP}_3$ , (b) monolayer  $\text{CaAs}_3$  and (c) monolayer  $\text{BaAs}_3$ . The  $\Lambda$  valley becomes the conduction band minimum for  $\text{BaAs}_3$ .

at  $\Gamma$  while the band gap of 1L BaAs<sub>3</sub> is indirect with the conduction band minimum (CBM) between  $S$  and  $\Gamma$ . The valence band of the  $G_0W_0$  band structure shows slightly lower dispersion than that of the PBE band structure. The stronger dispersion of the PBE band structure is due to the underestimation of the band gap, which is consistent with the trend for other semiconductors<sup>53</sup> and can be rationalized in terms of a  $k\cdot p$  theory that predicts  $m^* \propto E_g$  scaling (see ref. 54, p. 71). Apart from the dispersion, the band gap correction is the only noticeable difference between the band structures obtained with PBE and  $G_0W_0$ . The pDOS shows that the valence band edge is almost entirely composed of As 4p or P 3p orbitals, with the type 2 atoms (adjacent to cations) making up the major part. The conduction band edge is again primarily composed of As 4p (P 3p) states, As 4s (P 3s) and metal d states.

We next discuss the indirect nature of the band gap in 1L BaAs<sub>3</sub> *versus* the direct band gap in 1L CaAs<sub>3</sub>. An interesting feature in the band structure of 1L CaAs<sub>3</sub> is the local CBM between  $S$  and  $\Gamma$  at  $k_x = 1/3$ ,  $k_y = 1/3$ ,  $k_z = 0$  which we shall call  $\Lambda$

(see Fig. 3b). The same valley ( $\Lambda$ ) is the global CBM for 1L BaAs<sub>3</sub>. We want to shed light on why the  $\Lambda$  valley is more stable with respect to the  $\Gamma$  valley in 1L BaAs<sub>3</sub> but not in 1L CaAs<sub>3</sub>.

To that end, we analysed the orbital composition of the two valleys and then classified the interaction between the orbitals into bonding and antibonding by looking at the spatial distribution of the projected charge densities. From the pDOS we know that the valence band edge is almost entirely composed of As-2 4p orbitals. Fig. 4(a) shows the projected charge density of the topmost valence band at the  $\Gamma$  point for 1L CaAs<sub>3</sub>. The charge density distribution shows a clear p character with lobes of adjacent atoms avoiding each other. This suggests that the p-p interaction is antibonding. The conduction band edge (CBE) is mainly composed of As 4p, As 4s and metal d states. The projected charge density of the conduction band edge at  $\Lambda$  for 1L CaAs<sub>3</sub> is shown in Fig. 4(c). The As-2 4p-Ca 3d orbital contributions are hybridized and appear as lobes of charge density in Fig. 4(c) (see also Fig. S6 of the ESI†). From the spatial distribution of the charge density we can infer that the

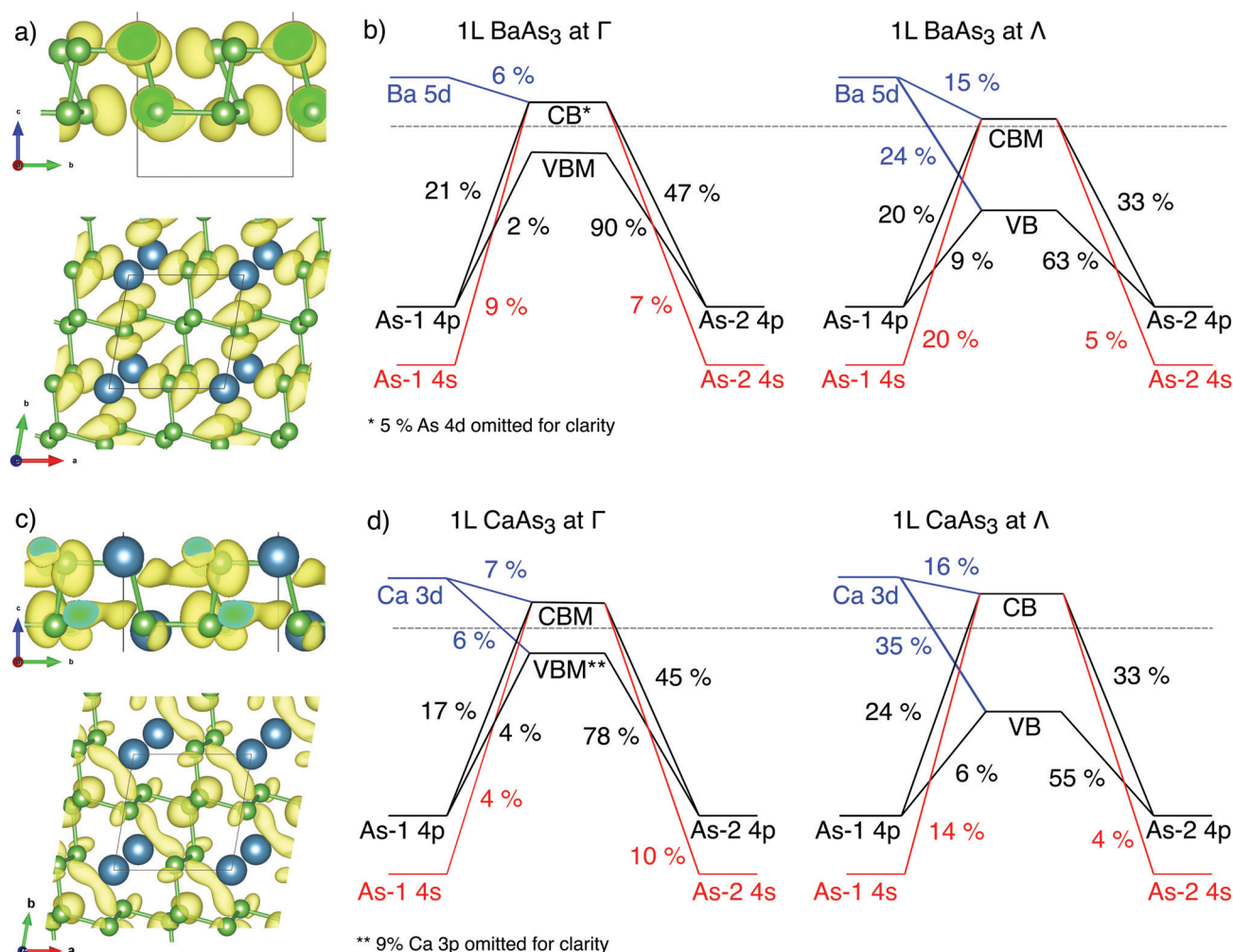


**Fig. 4** Orbital coupling in 1L CaAs<sub>3</sub> and 1L BaAs<sub>3</sub>. (a) Band and  $k$  point projected charge density of 1L CaAs<sub>3</sub> for the valence band at the  $\Gamma$  point. The isosurface is set at  $0.004 \text{ e} \text{\AA}^{-3}$ . (c) Band and  $k$  point projected charge density for the conduction bands at the  $\Lambda$  point. Isosurface:  $0.004 \text{ e} \text{\AA}^{-3}$ . (b) and (d) show schematics of the orbital coupling at the  $\Gamma$  and  $\Lambda$  points for 1L BaAs<sub>3</sub> and 1L CaAs<sub>3</sub>, respectively.

hybridized As-2 4p–Ca 3d states at the CBE interact in a bonding fashion, while As-1 states are not involved. The same holds true for BaAs<sub>3</sub> (see Fig. S7 and S8 of the ESI†).

In addition to analysis of the projected charge density, crystal orbital Hamilton population (COHP) bonding analysis was performed using LOBSTER,<sup>55–58</sup> which proved helpful to confirm the general picture of the antibonding nature at the valence and conduction band edges. However, the LOBSTER results are not shown because the current basis sets cannot project the empty d states of Ca and Ba. The COHP analysis of the parent structures, arsenene and phosphorene, also clearly shows the antibonding nature of the p–p interaction at the valence and conduction band edge (see the ESI,† Fig. S10 and S11).

Using the results of the bonding analysis we can create a schematic diagram of the coupling between As orbitals and Ca and Ba d orbitals as shown in Fig. 4(b) and (d). In comparison with the  $\Gamma$  valley, the  $\Lambda$  valley of the conduction band has higher contributions of As s and metal d orbitals. For example, the conduction band of 1L BaAs<sub>3</sub> (1L CaAs<sub>3</sub>) at  $\Lambda$  is composed of 15.0% Ba 5d (16% Ca 3d) orbitals while the  $\Gamma$  valley is composed of only 6% Ba 5d (7% Ca 3d). Because the p–d interaction is of bonding nature, we can expect the state at  $\Lambda$  to be stabilized, *i.e.*, lower in energy with increasing d orbital contribution. However, this alone does not provide an explanation for why the band gap is indirect for 1L BaAs<sub>3</sub> but not for 1L CaAs<sub>3</sub>.

The indirect band gap of 1L BaAs<sub>3</sub> can be attributed to an increase in the strength of the p–d interaction from 1L CaAs<sub>3</sub> to 1L BaAs<sub>3</sub>. The Ba 5d orbital is more delocalized than the Ca 3d orbital because the electrons in the 5d orbital experience stronger screening from the nuclear charge. Thus, the Ba 5d states can hybridize more strongly with As 4p orbitals than Ca 3d. As a result, the stronger bonding d–p interactions in 1L BaAs<sub>3</sub> stabilize the  $\Lambda$  valley CB state more than the weaker interaction in 1L CaAs<sub>3</sub>. This more pronounced energy shift leads to an indirect band gap in 1L BaAs<sub>3</sub>. Checking the conduction band dispersion of a hypothetical 1L SrAs<sub>3</sub> (data not shown), we find a decreasing trend of the  $\Lambda$  valley energy with respect to  $\Gamma$  from the  $n = 3$  to the  $n = 5$  shell, *i.e.* from Ca 3d over Sr 4d to Ba 5d, which strengthens the p–d interaction argument.

Next, we compare the band structures of monolayer CaAs<sub>3</sub> and CaP<sub>3</sub> (Fig. 3). The conduction band of 1L CaP<sub>3</sub> shows a stronger dispersion than that of 1L CaAs<sub>3</sub>, which is consistent with the prediction of high electron mobilities in 1L CaP<sub>3</sub>.<sup>5</sup> 1L CaP<sub>3</sub> has a larger band gap than CaAs<sub>3</sub>. Interestingly, 1L CaP<sub>3</sub> does not show any local CBM at  $\Lambda$  between  $\Gamma$  and  $S$ . And this despite the fact that the Ca 3d orbitals contribute about 53% of the CB state at  $\Lambda$ , which is significantly more than that for 1L CaAs<sub>3</sub>. We attribute this difference in orbital composition and electronic structure to the increased asymmetry of the 1L CaP<sub>3</sub> structure. The lattice parameter  $a = 5.71 \text{ \AA}$  is larger than  $b = 5.56 \text{ \AA}$ , whereas for 1L CaAs<sub>3</sub> the parameters are almost identical with  $a \approx b \approx 5.97 \text{ \AA}$ . This distortion leads to considerable differences in the projected charge density at the band edges for 1L CaP<sub>3</sub> (see the ESI,† Fig. S9).

Finally, we would like to note a similarity between the electronic structure of 1L CaP<sub>3</sub>, CaAs<sub>3</sub>, BaAs<sub>3</sub> and that of hybrid halide

perovskites. Specifically, both the top of the valence band and bottom of the conduction band are dominated by antibonding orbitals.<sup>59,60</sup> Defect tolerance properties inherent to hybrid halide perovskites are attributed to this feature.<sup>61–63</sup> Thus, we can anticipate 1L CaP<sub>3</sub>, CaAs<sub>3</sub> and BaAs<sub>3</sub> to exhibit a similar tolerance to native defects since states associated with dangling bonds are expected to appear within the bulk of valence or conduction band states rather than in the band gap.

## 4 Conclusion

In this work, we calculated the band alignment of puckered CaP<sub>3</sub>, CaAs<sub>3</sub> and BaAs<sub>3</sub> monolayers at the  $G_0W_0$  level of theory for the isolated monolayers according to the electron affinity rule. Our calculations suggest that monolayer CaP<sub>3</sub>, CaAs<sub>3</sub> and BaAs<sub>3</sub> all form type-II (staggered) heterojunctions which makes them suitable candidates for solar cell applications. Their quasi-particle gaps are 2.1 (direct), 1.8 (direct) and 1.5 eV (indirect), respectively. The differences in alignment with respect to the vacuum potential (*i.e.* the conduction band offsets) follow a trend in the chemical composition and also depend on the degree of relative stretching of the As or P anionic mesh upon insertion of the Ca or Ba ions. We also discussed trends in the electronic structure in the light of chemical bonding analysis. We found that the indirect band gap in BaAs<sub>3</sub> is caused by relatively strong As 3p–Ba 5d bonding interactions that stabilize the conduction band at  $\Lambda$ . Our study demonstrates the effect of structural distortion and orbital interactions on the theoretical band alignment of CaP<sub>3</sub>, CaAs<sub>3</sub> and BaAs<sub>3</sub>. These insights provide guidance for the future development of 2D heterojunctions based on phosphorene-like materials.

## Author contributions

M. L. conceived the idea in discussions with O. R. and H. S. M. L. performed the calculations and data analysis. H. S. contributed to the preparation of the monolayer structure files and heterostructure calculations. The manuscript was written by M. L., revised by O. R. and reviewed by H. S. The project was supervised by O. R.

## Conflicts of interest

There are no conflicts to declare.

## Acknowledgements

The authors acknowledge funding provided by the Natural Sciences and Engineering Research Council of Canada under the Discovery Grant Programs RGPIN-2020-04788. Calculations were performed using the Compute Canada infrastructure supported by the Canada Foundation for Innovation under John R. Evans Leaders Fund.

## References

- 1 L. Li, Y. Yu, G. J. Ye, Q. Ge, X. Ou, H. Wu, D. Feng, X. H. Chen and Y. Zhang, *Nat. Nanotechnol.*, 2014, **9**, 372–377.
- 2 V. Tran, R. Soklaski, Y. Liang and L. Yang, *Phys. Rev. B: Condens. Matter Mater. Phys.*, 2014, **89**, 235319.
- 3 P. Tang, J.-H. Yuan, Y.-Q. Song, M. Xu, K.-H. Xue and X.-S. Miao, *J. Mater. Sci.*, 2019, **54**, 12676–12687.
- 4 F. Li, H. Wu, Z. Meng, R. Lu and Y. Pu, *J. Phys. Chem. Lett.*, 2019, **10**, 761–767.
- 5 N. Lu, Z. Zhuo, H. Guo, P. Wu, W. Fa, X. Wu and X. C. Zeng, *J. Phys. Chem. Lett.*, 2018, **9**, 1728–1733.
- 6 Y. Jing, Y. Ma, Y. Li and T. Heine, *Nano Lett.*, 2017, **17**, 1833–1838.
- 7 A. Jalil, Z. Zhuo, Z. Sun, F. Wu, C. Wang and X. Wu, *J. Mater. Chem. A*, 2020, **8**, 1307–1314.
- 8 N. Miao, B. Xu, N. C. Bristowe, J. Zhou and Z. Sun, *J. Am. Chem. Soc.*, 2017, **139**, 11125–11131.
- 9 H.-Y. Liu, C.-L. Yang, M.-S. Wang and X.-G. Ma, *Appl. Surf. Sci.*, 2020, **501**, 144263.
- 10 G. Gaddemanne, W. G. Vandenberghe, M. L. Van de Put, S. Chen, S. Tiwari, E. Chen and M. V. Fischetti, *Phys. Rev. B*, 2018, **98**, 115416.
- 11 L. Cheng, C. Zhang and Y. Liu, *Phys. Rev. Lett.*, 2020, **125**, 177701.
- 12 A. J. Garza and G. E. Scuseria, *J. Phys. Chem. Lett.*, 2016, **7**, 4165–4170.
- 13 F. Hüser, T. Olsen and K. S. Thygesen, *Phys. Rev. B: Condens. Matter Mater. Phys.*, 2013, **87**, 235132.
- 14 H. Jiang, *J. Phys. Chem. C*, 2012, **116**, 7664–7671.
- 15 D. S. Koda, F. Bechstedt, M. Marques and L. K. Teles, *Phys. Rev. B*, 2018, **97**, 165402.
- 16 Y. Guo and J. Robertson, *Appl. Phys. Lett.*, 2016, **108**, 233104.
- 17 M.-H. Chiu, W.-H. Tseng, H.-L. Tang, Y.-H. Chang, C.-H. Chen, W.-T. Hsu, W.-H. Chang, C.-I. Wu and L.-J. Li, *Adv. Funct. Mater.*, 2017, **27**, 1603756.
- 18 W. Bauhofer, M. Wittmann and H. G. V. Schnerring, *J. Phys. Chem. Solids*, 1981, **42**, 687–695.
- 19 W. Dahlmann and H. G. V. Schnerring, *Naturwissenschaften*, 1973, **60**, 518.
- 20 G. Kresse and J. Furthmüller, *Phys. Rev. B: Condens. Matter Mater. Phys.*, 1996, **54**, 11169–11186.
- 21 G. Kresse and J. Furthmüller, *Comput. Mater. Sci.*, 1996, **6**, 15–50.
- 22 P. E. Blöchl, *Phys. Rev. B: Condens. Matter Mater. Phys.*, 1994, **50**, 17953–17979.
- 23 G. Kresse and D. Joubert, *Phys. Rev. B: Condens. Matter Mater. Phys.*, 1999, **59**, 1758–1775.
- 24 J. P. Perdew, K. Burke and M. Ernzerhof, *Phys. Rev. Lett.*, 1996, **77**, 3865–3868.
- 25 S. Grimme, J. Antony, S. Ehrlich and H. Krieg, *J. Chem. Phys.*, 2010, **132**, 154104.
- 26 O. A. Vydrov and T. Van Voorhis, *J. Chem. Phys.*, 2010, **133**, 244103.
- 27 P. Giannozzi, S. Baroni, N. Bonini, M. Calandra, R. Car, C. Cavazzoni, D. Ceresoli, G. L. Chiarotti, M. Cococcioni, I. Dabo, A. D. Corso, S. D. Gironcoli, S. Fabris, G. Fratesi, R. Gebauer, U. Gerstmann, C. Gougoussis, A. Kokalj, M. Lazzeri, L. Martin-Samos, N. Marzari, F. Mauri, R. Mazzarello, S. Paolini, A. Pasquarello, L. Paulatto, C. Sbraccia, S. Scandolo, G. Sclauzero, A. P. Seitsonen, A. Smogunov, P. Umari and R. M. Wentzcovitch, *J. Phys.: Condens. Matter*, 2009, **21**, 395502.
- 28 M. J. van Setten, M. Giantomassi, E. Bousquet, M. J. Verstraete, D. R. Hamann, X. Gonze and G. M. Rignanese, *Comput. Phys. Commun.*, 2018, **226**, 39–54.
- 29 M. S. Hybertsen and S. G. Louie, *Phys. Rev. B: Condens. Matter Mater. Phys.*, 1986, **34**, 5390–5413.
- 30 M. Rohlfing and S. G. Louie, *Phys. Rev. B: Condens. Matter Mater. Phys.*, 2000, **62**, 4927–4944.
- 31 J. Deslippe, G. Samsonidze, D. A. Strubbe, M. Jain, M. L. Cohen and S. G. Louie, *Comput. Phys. Commun.*, 2012, **183**, 1269–1289.
- 32 J. Deslippe, G. Samsonidze, M. Jain, M. L. Cohen and S. G. Louie, *Phys. Rev. B: Condens. Matter Mater. Phys.*, 2013, **87**, 165124.
- 33 S. Ismail-Beigi, *Phys. Rev. B: Condens. Matter Mater. Phys.*, 2006, **73**, 233103.
- 34 F. H. da Jornada, D. Y. Qiu and S. G. Louie, *Phys. Rev. B*, 2017, **95**, 035109.
- 35 D. Y. Qiu, F. H. da Jornada and S. G. Louie, *Nano Lett.*, 2017, **17**, 4706–4712.
- 36 J. Lu, J. Yang, A. Carvalho, H. Liu, Y. Lu and C. H. Sow, *Acc. Chem. Res.*, 2016, **49**, 1806–1815.
- 37 L. Liang, J. Wang, W. Lin, B. G. Sumpter, V. Meunier and M. Pan, *Nano Lett.*, 2014, **14**, 6400–6406.
- 38 H. Shu and J. Guo, *Mater. Res. Express*, 2018, **5**, 036302.
- 39 D. Kecik, E. Durgun and S. Ciraci, *Phys. Rev. B*, 2016, **94**, 205409.
- 40 X. Niu, Y. Li, Q. Zhou, H. Shu and J. Wang, *ACS Appl. Mater. Interfaces*, 2017, **9**, 42856–42861.
- 41 A. A. Mostofi, J. R. Yates, G. Pizzi, Y.-S. Lee, I. Souza, D. Vanderbilt and N. Marzari, *Comput. Phys. Commun.*, 2014, **185**, 2309–2310.
- 42 K. Momma and F. Izumi, *J. Appl. Crystallogr.*, 2011, **44**, 1272–1276.
- 43 A. Kokalj, *J. Mol. Graph. Model.*, 1999, **17**, 176–179.
- 44 V. Wang, N. Xu, J. C. Liu, G. Tang and W.-T. Geng, 2020, arXiv:1908.08269v5 [cond-mat.mtrl-sci].
- 45 Y. Liang, S. Huang, R. Soklaski and L. Yang, *Appl. Phys. Lett.*, 2013, **103**, 042106.
- 46 *MoS<sub>2</sub>: Materials, Physics, and Devices*, ed. Z. M. Wang, Springer International Publishing, Cham, 2014, vol. 21.
- 47 A. Slăss, S. M. Gali, A. Pershin, A. Gali, J. Cornil and D. Beljonne, *J. Phys. Chem. Lett.*, 2020, **11**, 4503–4510.
- 48 R. L. Anderson, *IBM J. Res. Dev.*, 1960, **4**, 283–287.
- 49 D. S. Koda, F. Bechstedt, M. Marques and L. K. Teles, *J. Phys. Chem. C*, 2017, **121**, 3862–3869.
- 50 U. Herath, P. Tavadze, X. He, E. Bousquet, S. Singh, F. Muñoz and A. H. Romero, *Comput. Phys. Commun.*, 2020, **251**, 107080.
- 51 D. Jariwala, A. R. Davoyan, J. Wong and H. A. Atwater, *ACS Photonics*, 2017, **4**, 2962–2970.

- 52 Y. Lv, W. Qin, C. Wang, L. Liao and X. Liu, *Adv. Electron. Mater.*, 2019, **5**, 1800569.
- 53 O. Rubel, F. Tran, X. Rocquefelte and P. Blaha, *Comput. Phys. Commun.*, 2020, 107648.
- 54 P. Y. Yu and M. Cardona, *Fundamentals of Semiconductors*, Springer Berlin Heidelberg, Berlin, Heidelberg, 2010.
- 55 R. Nelson, C. Ertural, J. George, V. L. Deringer, G. Hautier and R. Dronskowski, *J. Comput. Chem.*, 2020, **41**, 1931–1940.
- 56 V. L. Deringer, A. L. Tchougréeff and R. Dronskowski, *J. Phys. Chem. A*, 2011, **115**, 5461–5466.
- 57 S. Maintz, V. L. Deringer, A. L. Tchougréeff and R. Dronskowski, *J. Comput. Chem.*, 2013, **34**, 2557–2567.
- 58 R. Dronskowski and P. E. Bloechl, *J. Phys. Chem.*, 1993, **97**, 8617–8624.
- 59 T. Umebayashi, K. Asai, T. Kondo and A. Nakao, *Phys. Rev. B: Condens. Matter Mater. Phys.*, 2003, **67**, 155405.
- 60 S. Tao, I. Schmidt, G. Brocks, J. Jiang, I. Tranca, K. Meerholz and S. Olthof, *Nat. Commun.*, 2019, **10**, 2560.
- 61 J. Kim, S.-H. Lee, J. H. Lee and K.-H. Hong, *J. Phys. Chem. Lett.*, 2014, **5**, 1312–1317.
- 62 W.-J. Yin, T. Shi and Y. Yan, *Appl. Phys. Lett.*, 2014, **104**, 063903.
- 63 C. Zheng, O. Rubel, M. Kepenekian, X. Rocquefelte and C. Katan, *J. Chem. Phys.*, 2019, **151**, 234704.

**Supplementary information: Band alignment of monolayer CaP<sub>3</sub>, CaAs<sub>3</sub>,  
BaAs<sub>3</sub> and the role of *p-d* orbital interactions in the formation of conduction  
band minima**

Magdalena Laurien,<sup>1,\*</sup> Himanshu Saini,<sup>1</sup> and Oleg Rubel<sup>1,†</sup>

<sup>1</sup>*Department of Materials Science and Engineering, McMaster University,  
1280 Main Street West, Hamilton, Ontario L8S 4L7, Canada*

(Dated: March 4, 2021)

## I. VASP STRUCTURE FILES (POSCAR)

CaAs3 monolayer

1.000000000000000  
5.967380046799998 0.000000000000000 0.000000000000000  
1.016573236300000 5.880315464999998 0.000000000000000  
0.000000000000000 0.000000000000000 26.000000000000000

Ca As

2 6

Direct

0.1769423339673324 0.1774698642655252 0.0843192194397560  
0.0000016750081002 0.0000031145587513 0.1923299163679317  
0.5550182146338116 0.5553423423773509 0.0925341103014574  
0.6648516406207534 0.1335817668416936 0.0944098219129259  
0.1332745527381149 0.6653217049443185 0.0944285201829231  
0.0436701687153871 0.5121502125423447 0.1822206247786156  
0.5120924785388894 0.0438910346111427 0.1822393138947689  
0.6219257947279928 0.6221305888304300 0.1841156215831603

CaP3 monolayer

1.0

5.7089400291	0.0000000000	0.0000000000
0.9168738936	5.4873170208	0.0000000000
0.0000000000	0.0000000000	26.0000000000

Ca P

2 6

Direct

0.990673363	0.236208677	0.069827832
0.000045002	0.000023723	0.192322791
0.504078567	0.176318109	0.089228347
0.436399102	0.576579750	0.091769300
0.052144825	0.713358402	0.095917709
0.938541174	0.522884250	0.166239306
0.554308176	0.659748256	0.170394331
0.486642480	0.060008407	0.172931165

BaAs3 monolayer

1.00000000000000

6.458119869199999 0.000000000000000 0.000000000000000

1.840688298299999 6.190248689199997 0.000000000000000

0.000000000000000 0.000000000000000 26.000000000000000

Ba As

2 6

Direct

0.1707610055466162 0.1707610052636852 0.0600013274230804

0.000000000000000 0.000000000000000 0.1923033457692327

0.5351630050496041 0.5351629619953329 0.0825415574615391

0.6681529921206035 0.1361709981814840 0.0858069291538470

0.1361710152654183 0.6681529718209944 0.0858069291538470

0.5026080206547903 0.0345905004387888 0.1664977440384590

0.0345905056370839 0.5026080011014997 0.1664977440384590

0.6355980209158645 0.6355979338704856 0.1697630882307664

Black phosphorene

1.00000000000000

4.5905542594727189 0.0000000000000000 0.0000000000000000

0.0000000000000000 3.2953912493002919 0.0000000000000000

0.0000000000000000 0.0000000000000000 24.6571569442999987

P

4

Direct

0.4116710144483093 0.0000000000000000 0.2588742328996148

0.5883289855290670 0.0000000000000000 0.1733393012103477

0.0883289707180026 0.5000000001209344 0.2588742328996148

0.9116710143238436 0.5000000001209344 0.1733393012103477

Puckered arsenene

1.00000000000000

4.6805338045812581 0.0000000000000000 0.0000000000000000

0.0000000000000000 3.6968139797539545 0.0000000000000000

0.0000000000000000 0.0000000000000000 24.0000000000000000

As

4

Direct

0.0687993159732372 0.0000000000000000 0.5501907684701308

0.9312007138572724 0.0000000000000000 0.4498092191132059

0.4312006842174441 0.4999999999591296 0.5501907684701308

0.5687992860791624 0.4999999999591296 0.4498092191132059

## II. WANNIER INTERPOLATION OF THE BAND STRUCTURES

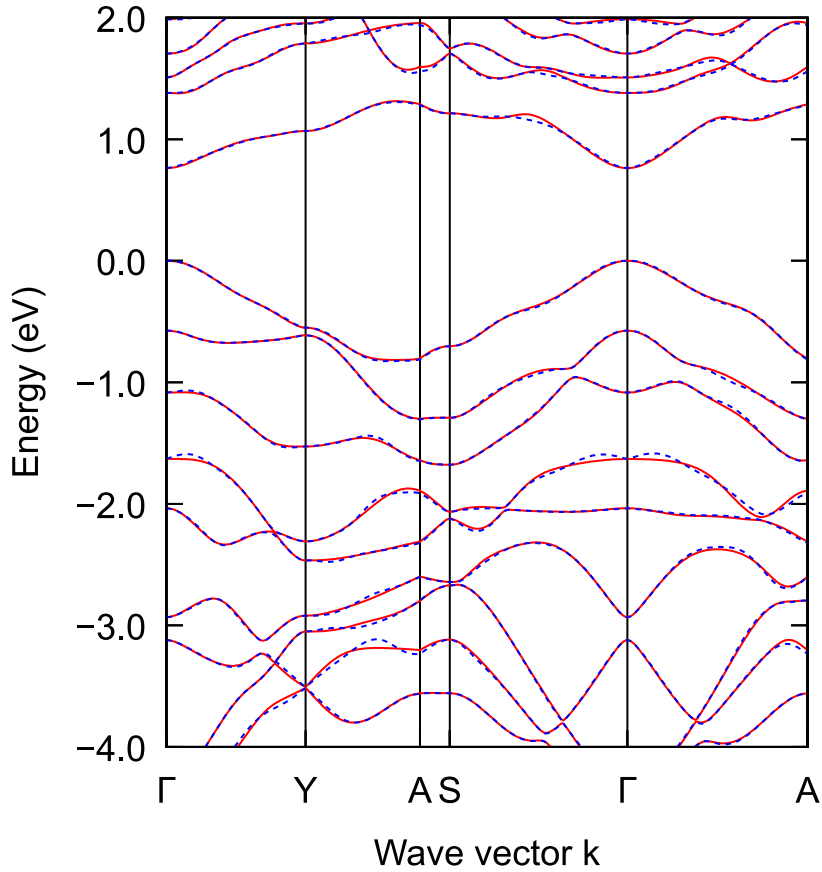


FIG. S1: PBE band structure of CaP<sub>3</sub>. The red lines show the bandstructure obtained along a  $k$  path from Quantum Espresso<sup>1</sup>, the blue dashed lines show the wannier interpolation along the same path from a  $6 \times 6 \times 1$   $k$  grid. The wannierization was performed with wannier90<sup>2</sup> for 100 iterations using random projections with 45 bands (20 valence and 25 conduction bands, each) as input to obtain 45 wannier functions.

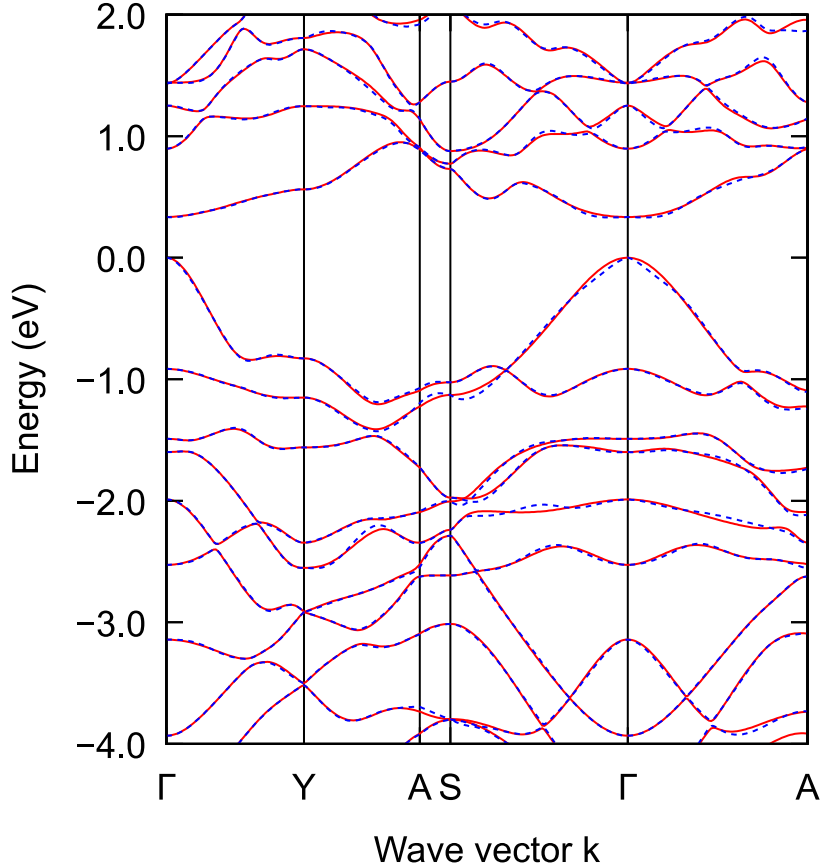


FIG. S2: PBE band structure of CaAs<sub>3</sub>. The red lines show the bandstructure obtained along a  $k$  path from Quantum Espresso, the blue dashed lines show the wannier interpolation along the same path from a  $6 \times 6 \times 1$   $k$  grid. The wannierization was performed with wannier90 for 100 iterations using random projections with 40 bands (20 valence and 20 conduction bands, each) as input to obtain 40 wannier functions.

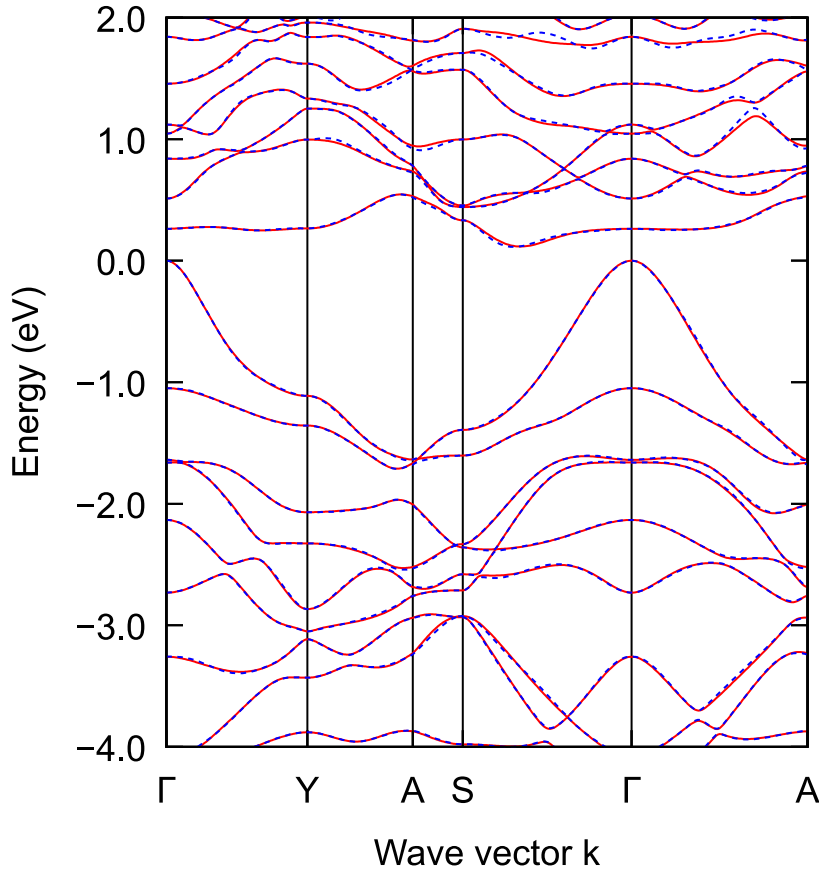


FIG. S3: PBE band structure of BaAs<sub>3</sub>. The red lines show the bandstructure obtained along a  $k$  path from Quantum Espresso, the blue dashed lines show the wannier interpolation along the same path from a  $6 \times 6 \times 1$   $k$  grid. The wannierization was performed with wannier90 for 100 iterations using random projections with 40 bands (20 valence and 20 conduction bands, each) as input to obtain 40 wannier functions.

### III. CALCIUM TRIARSENIDE / CALCIUM TRIPHOSPHIDE HETEROSTRUCTURE

To estimate the effect of charge transfer and band shifts in a heterojunction, we calculated the band alignment of a basic  $\text{CaAs}_3/\text{CaP}_3$  heterostructure at the PBE level using VASP<sup>11-15</sup> (see Fig. S4). We note that for more accurate results, non-local effects should be included by using hybrid functionals.<sup>3</sup> The figure shows the band alignment with respect to the vacuum level (set to zero) of the unstrained monolayers, strained monolayers and the heterostructure consisting of the strained monolayers. The band alignment of the unstrained and strained monolayers reflect the alignment according to the electron affinity rule. The atom-projected band structure of the heterostructure is shown in Figure S5.

To create a heterostructure, we apply strain of less than 5 % in each direction, compressing  $\text{CaAs}_3$  and straining  $\text{CaP}_3$ . As a result of the strain, the band gap of  $\text{CaAs}_3$  decreases from 0.33 eV to 0.10 eV and the band gap of  $\text{CaP}_3$  increases from 0.75 eV to 0.90 eV. The strained monolayers form a type-I heterojunction according the the electron affinity rule.

Combining the strained monolayers in a heterostructure leads to an overall downshift of the bands with respect the vacuum level. However, the relative band alignments are only slightly affected by creating a heterostructure. Also, the respective band gaps of the heterostructure do not close significantly compared to the strained monolayers. In effect, this means that there is a weaker dependence of the band gap on number of layers in the heterostructure than in a homo-bilayer.<sup>4,5</sup>

Further, weak to moderate hybridization of the valence and conduction band occurs which is due to overlap of the out-of-plane  $p_z$  and  $d_{z^2}$  orbital contributions. The weak nature of the hybridization allows us to still define proper band offsets. We also observe a charge transfer from  $\text{CaP}_3$  to  $\text{CaAs}_3$ , which is indicated by the step in the vacuum level of -0.2 eV. Overall, the electron affinity rule predicts the band alignment of the heterostructure rather well for this  $\text{CaAs}_3/\text{CaP}_3$  heterostructure.

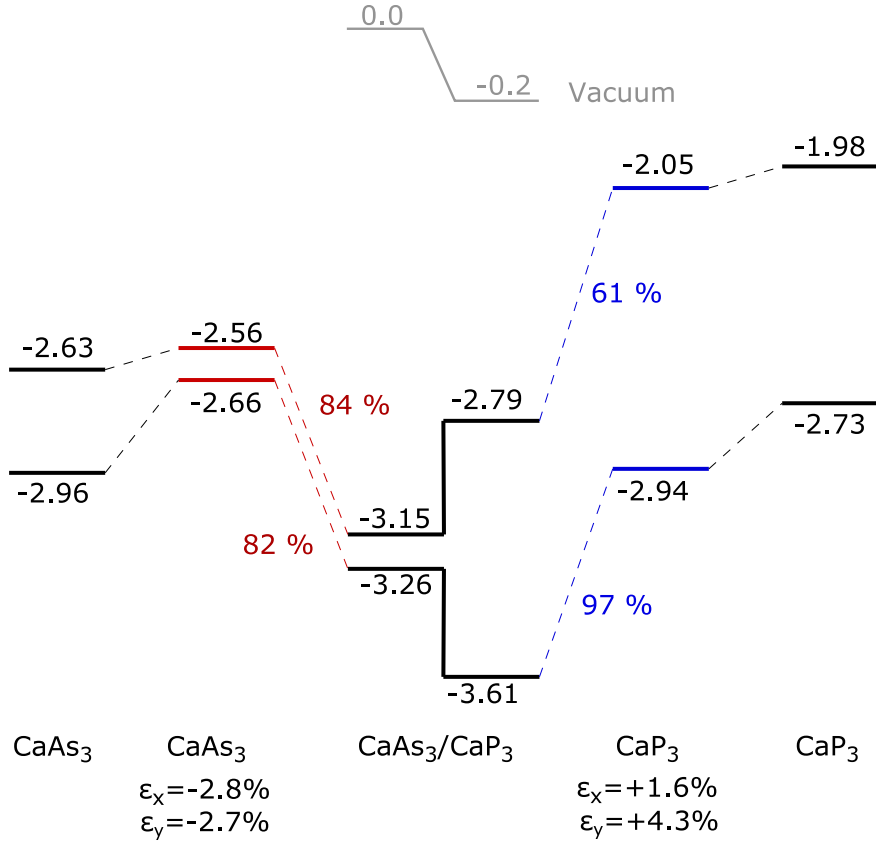


FIG. S4: Band alignment of the CaAs<sub>3</sub>/CaP<sub>3</sub> heterostructure calculated with the PBE-D3 functional in VASP. The bands are aligned with respect to the vacuum level (set to zero) with values given in eV. Shown are the valence and conduction band at  $\Gamma$  of the fully relaxed monolayer, strained monolayer and for the heterostructure. Contributions to a state of the heterostructure are indicated as percentages along the dashed lines. The charge transfer from CaP<sub>3</sub> to CaAs<sub>3</sub> is evident from the step of the vacuum level introduced in the heterostructure.

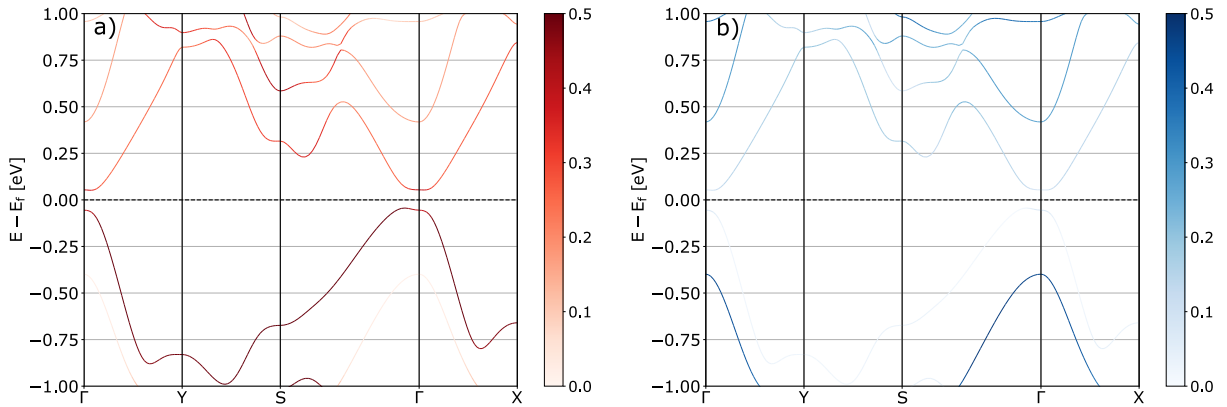


FIG. S5: PBE band structure of the CaAs<sub>3</sub>/CaP<sub>3</sub> heterostructure. a) Projected contribution of CaAs<sub>3</sub>, b) projected contribution of CaP<sub>3</sub>. The valence and conduction band are dominated by CaAs<sub>3</sub> while the immediate neighbouring bands are dominated by CaP<sub>3</sub>. The band gap of the heterostructure is slightly indirect. The figures were obtained with the help of the pyproc<sup>6</sup> tool.

#### IV. PROJECTED DENSITY OF STATES

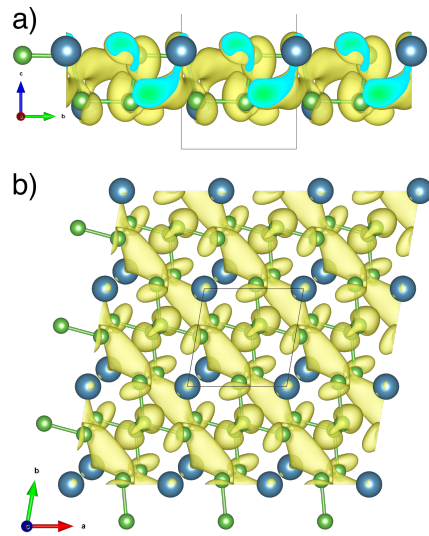


FIG. S6: a,b) Band and  $k$  point projected charge density of 1L CaAs<sub>3</sub> at the conduction band at  $\Lambda$ . The isosurface is set at 0.0025 e/Å<sup>3</sup>. At this isosurface level, the connection of the charge density lobes to the Ca atoms can be clearly seen.

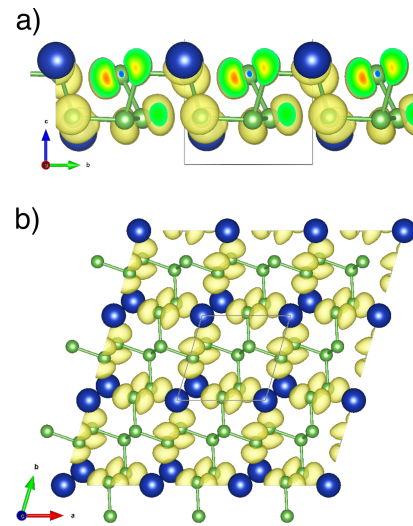


FIG. S7: a,b) Band and  $k$  point projected charge density of 1L BaAs<sub>3</sub> for the valence band at the  $\Gamma$  point. Isosurface: 0.004 e/Å<sup>3</sup>.

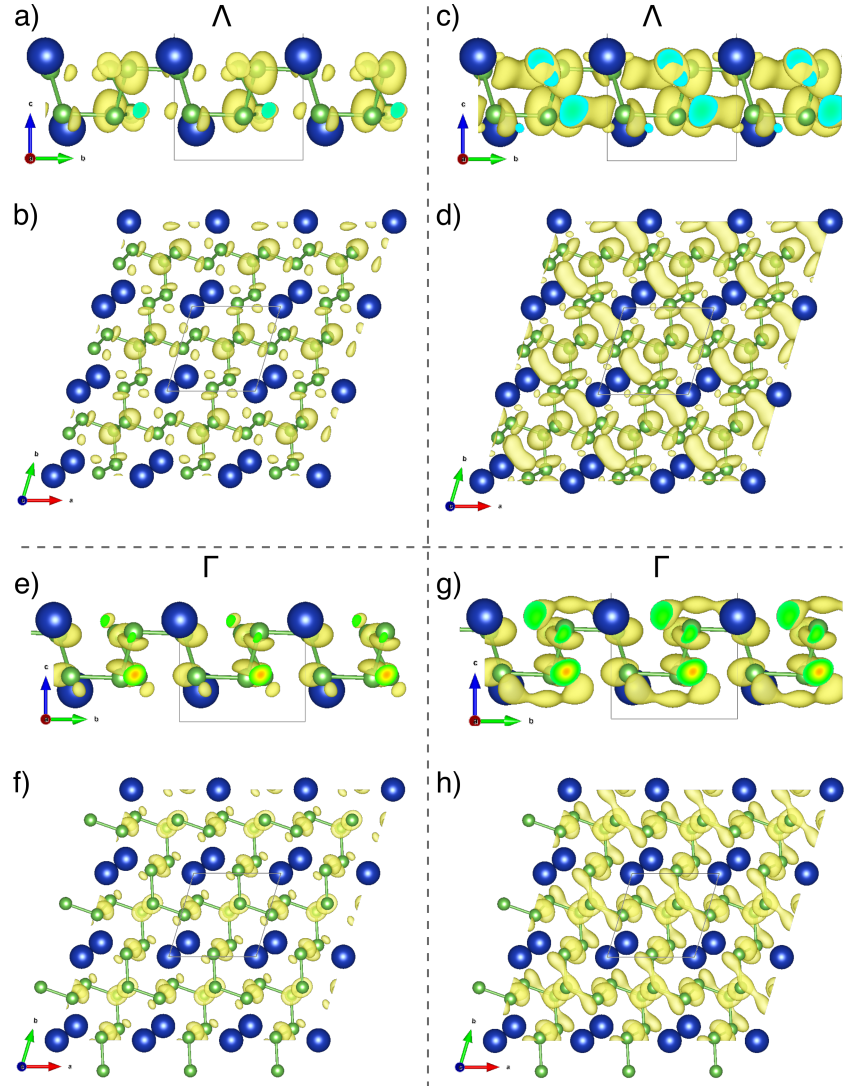


FIG. S8: a-d) Band and  $k$  point projected charge density of 1L  $\text{BaAs}_3$  for the conduction band at  $\Lambda$ . The isosurface is set a,b)  $0.004 \text{ e}/\text{\AA}^3$  and c,d)  $0.0025 \text{ e}/\text{\AA}^3$ . The 5d orbital of Ba is strongly delocalized. Because the d orbital is more spread out, the lobes become visible at an isosurface of  $0.0025 \text{ e}/\text{\AA}^3$  only. For comparison the band and  $k$  point projected charge density for the conduction band at the  $\Gamma$  point is shown in e-h). Isosurface: e,f)  $0.004 \text{ e}/\text{\AA}^3$ , g,h)  $0.0025 \text{ e}/\text{\AA}^3$ .

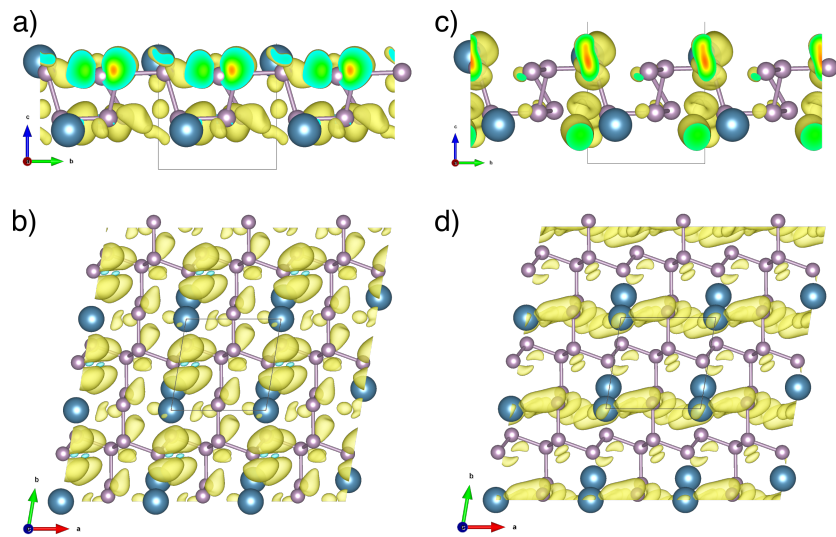


FIG. S9: a,b) Band and  $k$  point projected charge density of 1L  $\text{CaP}_3$  for the valence band at the  $\Gamma$  point. The isosurface is set at  $0.004 \text{ e}/\text{\AA}^3$ . c,d) Band and  $k$  point projected charge density for the conduction bands at the  $\Lambda$  point. Isosurface:  $0.004 \text{ e}/\text{\AA}^3$ .

## V. BONDING ANALYSIS OF PUCKERED PHOSPHORENE AND ARSENENE

The partial density of states (pDOS) and crystal orbital hamilton populations (COHP) were obtained using LOBSTER<sup>7-10</sup> with input from VASP PBE calculations<sup>11-15</sup>. From analysing pDOS and COHP, the orbital composition of the electronic structure and their bonding/antibonding nature can be obtained. The positive -COHP axis denotes bonding character of the covalent bonds and the negative -COHP axis antibonding character. The DOS and COHP of black phosphorene and puckered arsenene are shown in Fig. S10 and Fig. S11, respectively. We see that both the valence band edge and the conduction band edge the of phosphorene and arsenene have *p* character. The *p-p* interaction is slightly antibonding at the valence band edge and strongly antibonding for the conduction band, which is apparent from the COHP analysis.

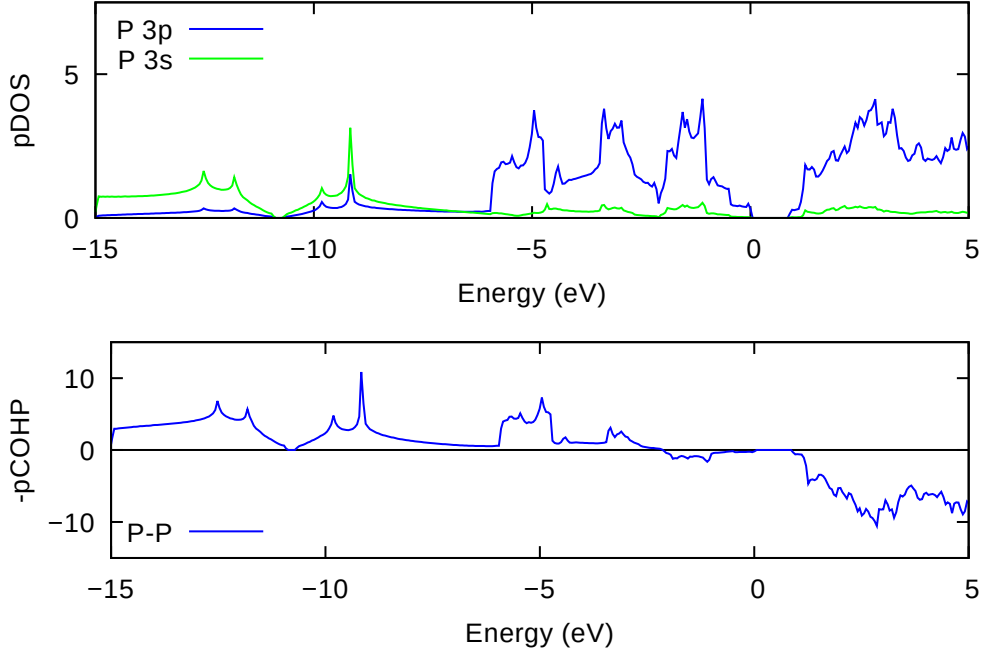


FIG. S10: Density of states (DOS) and bonding indicator (pCOHP) of black phosphorene. The energy of the valence band maximum is set to zero.

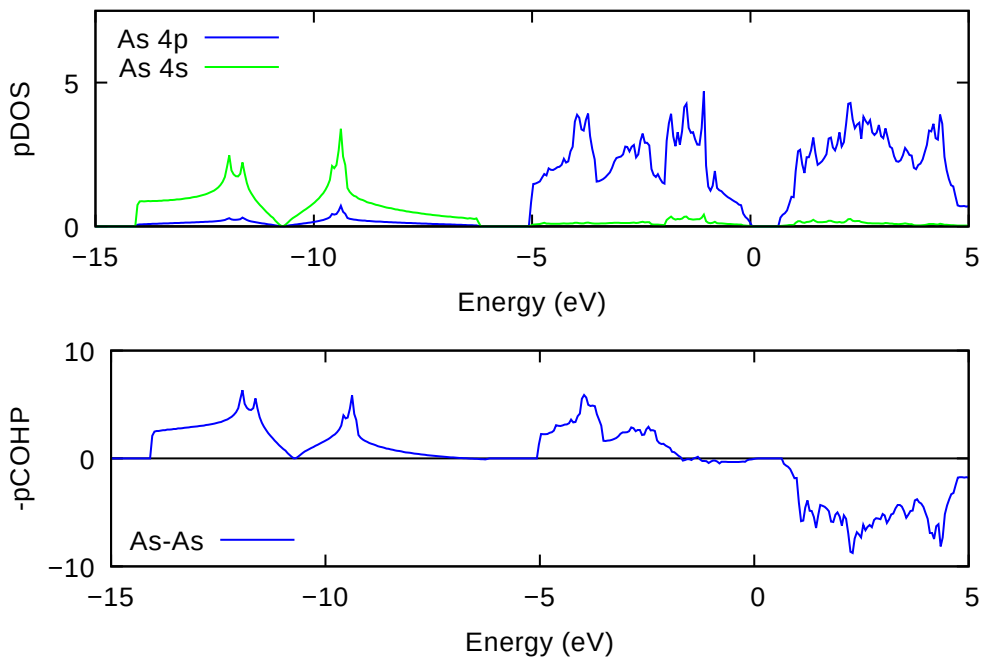


FIG. S11: Density of states (DOS) and bonding indicator (pCOHP) of puckered arsenene. The energy of the valence band maximum is set to zero.

---

\* laurienm@mcmaster.ca

† rubelo@mcmaster.ca

- <sup>1</sup> P. Giannozzi, S. Baroni, N. Bonini, M. Calandra, R. Car, C. Cavazzoni, D. Ceresoli, G. L. Chiarotti, M. Cococcioni, I. Dabo, A. D. Corso, S. d. Gironcoli, S. Fabris, G. Fratesi, R. Gebauer, U. Gerstmann, C. Gougoussis, A. Kokalj, M. Lazzeri, L. Martin-Samos, N. Marzari, F. Mauri, R. Mazzarello, S. Paolini, A. Pasquarello, L. Paulatto, C. Sbraccia, S. Scandolo, G. Sclauzero, A. P. Seitsonen, A. Smogunov, P. Umari and R. M. Wentzcovitch, *J. Phys. : Condens. Matter.*, 2009, **21**, 395502.
- <sup>2</sup> A. A. Mostofi, J. R. Yates, G. Pizzi, Y.-S. Lee, I. Souza, D. Vanderbilt and N. Marzari, *Comput. Phys. Commun.*, 2014, **185**, 2309–2310.
- <sup>3</sup> D. S. Koda, F. Bechstedt, M. Marques and L. K. Teles, *Phys. Rev. B*, 2018, **97**, 165402.
- <sup>4</sup> N. Lu, Z. Zhuo, H. Guo, P. Wu, W. Fa, X. Wu and X. C. Zeng, *J. Phys. Chem. Lett.*, 2018, **9**, 1728–1733.
- <sup>5</sup> F. Li, H. Wu, Z. Meng, R. Lu and Y. Pu, *J. Phys. Chem. Lett.*, 2019, **10**, 761–767.
- <sup>6</sup> U. Herath, P. Tavadze, X. He, E. Bousquet, S. Singh, F. Muñoz and A. H. Romero, *Computer Physics Communications*, 2020, **251**, 107080.
- <sup>7</sup> R. Nelson, C. Ertural, J. George, V. L. Deringer, G. Hautier and R. Dronskowski, *J. Comput. Chem.*, 2020, **41**, 1931–1940.
- <sup>8</sup> V. L. Deringer, A. L. Tchougréeff and R. Dronskowski, *J. Phys. Chem. A*, 2011, **115**, 5461–5466.
- <sup>9</sup> S. Maintz, V. L. Deringer, A. L. Tchougréeff and R. Dronskowski, *J. Comput. Chem.*, 2013, **34**, 2557–2567.
- <sup>10</sup> R. Dronskowski and P. E. Blöchl, *J. Phys. Chem.*, 1993, **97**, 8617–8624.
- <sup>11</sup> G. Kresse and J. Furthmüller, *Phys. Rev. B*, 1996, **54**, 11169–11186.
- <sup>12</sup> G. Kresse and J. Furthmüller, *Comput. Mater. Sci.*, 1996, **6**, 15–50.
- <sup>13</sup> P. E. Blöchl, *Phys. Rev. B*, 1994, **50**, 17953–17979.
- <sup>14</sup> G. Kresse and D. Joubert, *Phys. Rev. B*, 1999, **59**, 1758–1775.
- <sup>15</sup> J. P. Perdew, K. Burke and M. Ernzerhof, *Phys. Rev. Lett.*, 1996, **77**, 3865–3868.